Quantifying Surface Reflectivity for Spaceborne Lidar via Two Independent Methods

Mathias I. Disney, Philip E. Lewis, Marc Bouvet, Ana Prieto-Blanco, and Steven Hancock

***Abstract*—Spaceborne differential absorption lidar has been proposed for accurate measurements of atmospheric CO_2 (and surface properties). Lidar instruments typically observe the highest possible surface reflectance due to observing in the retroreflection direction (the so-called "hotspot") where viewed shadow is minimized. The range of observed reflectance will determine instrument dimensions and signal-to-noise ratio, but it is difficult to predict this range globally *a priori*. Two complementary methods are presented for estimating lidar reflectivity over a range of vegetated surface types. The first method simulates the expected response of a lidar instrument from multiangle multispectral reflectance data. The second method uses detailed 3-D vegetation structural models and Monte Carlo ray tracing to simulate the lidar signal. The simulations are used to validate the first method and assess the impact of possible instrument configurations. Both methods agree well and are robust to error in observations, with predicted lidar reflectivity (at 1570 and 2050 nm here) typically between 10% and 33% higher relative to off-nadir reflectance and ranging from 0.02 to ∼0.7. We use the 3-D simulations to show that the impact of shifted on–off lidar pulses is not likely to be significant for accuracy of retrieved CO_2, and we demonstrate that the 3-D simulation method is a flexible and powerful way of prototyping future spaceborne lidar missions.**

***Index Terms*—Bidirectional reflectance distribution function (BRDF), hotspot, lidar, radiative transfer, 3-D modeling.**

I. Introduction

THERE is increasing interest in the possibility of using spaceborne differential absorption lidar (DIAL) to estimate atmospheric concentrations of CO_2, water vapor, and O_3 [1]–[3], as well as for measuring surface biophysical properties such as vegetation structure [4]–[6]. DIAL instruments have been widely used for airborne and ground-based measurements of atmospheric constituents but have yet to be deployed in space despite a number of advantages, including spatial coverage, and synergy with other ground-based and airborne profile measurements [1].

Manuscript received September 4, 2008; revised March 18, 2009. This work was supported in part by the Natural Environment Research Council (NERC) National Centre for Earth Observation (NE/F001444/1), by the NERC ABACUS project (NE/D005922/1), by the NERC Field Spectroscopy Facility, by ESA RFQ/3-12259/07/NL/JA, and by EPSRC Studentship GR/9054658.

M. I. Disney, P. E. Lewis, and A. Prieto-Blanco are with the Department of Geography, University College London, WC1E 6BT London, U.K. (e-mail: mdisney@geog.ucl.ac.uk; plewis@geog.ucl.ac.uk; prieto@geog.ucl.ac.uk).

M. Bouvet is with the Wave Interaction and Propagation Section, European Space Agency, European Space Research and Technology Centre, 2200 AG Noordwijk, The Netherlands (e-mail: marc.bouvet@esa.int).

S. Hancock is with the Department of Civil, Environmental and Geomatic Engineering, Department of Geography, and Department of Space and Climate Physics, University College London, WC1E 6BT London, U.K. (e-mail: shancock@geog.ucl.ac.uk).

Digital Object Identifier 10.1109/TGRS.2009.2019268

Lidar instruments have an advantage over solar-reflected instruments in that they can operate continuously, not just in daylight. Such instruments also have the capacity to measure atmospheric CO_2 at higher precision than current or proposed passive instruments, due to a higher signal-to-noise ratio than is possible with a solar-reflected signal [1], [5]. Spaceborne DIAL instruments may also provide information on surface biophysical properties such as vegetation structure (given certain choices of instrument configuration such as pulse duration and footprint size). DIAL instruments measure at two wavelengths: one located in an atmospheric absorption feature due to the desired compound (on pulse) and one at a reference (unabsorbed) wavelength (off pulse). The difference in absorption between the two pulses reflected from the surface allows estimation of the concentration of absorbing constituents in the instrument field of view (FOV). An example of such an instrument is the proposed ESA Advanced Space Carbon and Observation of Planet Earth (A-SCOPE) mission. A-SCOPE is designed to observe spatial and temporal gradients of atmospheric CO_2 with a precision and accuracy sufficient to constrain the CO_2 fluxes (sources and sinks) within 0.02 PgCyr^{-1} on a scale of 10^6 km^2 [2].

For a spaceborne lidar instrument, the viewing and illumination geometry are constrained to be in (or very close to) the so-called "hotspot," where the viewing and illumination vectors $\Omega(\theta_v, \varphi_v)$ and $\Omega'(\theta_i, \varphi_i)$ are coincident ($\theta_{v,i}$ are $\varphi_{v,i}$ are the view and illumination zenith and azimuth angles, respectively). Natural surfaces tend to exhibit a peak of reflectance at any hotspot configuration, largely due to the minimization of shadow viewed at this point (from geometric optic considerations)—hence the term "hotspot" [6]. This peak of reflectance, also known as the "opposition effect," can also be augmented by coherent scattering [7]. In this case, for a medium composed of scatterers of approximately the same size as the illuminating wavelength separated by gaps much larger than the wavelength, coherent multiple scattering can occur within the media, which acts to increase the reflected signal [8]. We ignore this effect here, as coherent scattering typically occurs over a very narrow range of phase angles, and in the case of vegetation, the scattering elements (and gaps) are far larger than the illuminating wavelength. In this case, macroscopic shadowing (due to objects far larger than the wavelength) will dominate the hotspot [8], [9].

For a spaceborne lidar, viewing and illumination would not only be coincident but would also be at or very close to nadir, i.e., the instrument would view in the nadir hotspot (or NHS). To determine instrument design and performance for a lidar of this sort, the likely limits of observed reflectivity at NHS

are required. The lower limit of reflectivity, for example, will largely determine the size of the instrument optics; the range of values (the difference between possible upper and lower values) will determine instrument sensitivity. Consequently, some way of accurately characterizing surface reflectivity in the NHS is required in order that choices about instrument design can be made accordingly.

The variation of surface reflectance as a function of view and illumination angles is described by the bidirectional reflectance distribution function (BRDF) defined as

$$BRDF_\lambda\left(\Omega(\theta_v,\varphi_v);\Omega'(\theta_i,\varphi_i)\right) = \frac{dL_{\lambda,v}\left(\Omega(\theta_v,\varphi_v);\Omega'(\theta_i,\varphi_i)\right)}{dE_{\lambda,i}\left(\Omega'(\theta_i,\varphi_i)\right)}[\mathrm{sr}^{-1}\cdot\mu\mathrm{m}^{-1}] \quad (1)$$

where $dL_{\lambda,v}$ and $dE_{\lambda,i}$ are infinitesimal increments in reflected (available for viewing) and incident radiation, respectively, through infinitesimally small solid angle. Since BRDF is a description over an infinitesimal solid angle and wavelength interval (implied by the λ subscript), it is not measurable in practice. In its place, the spectral bidirectional reflectance factor (BRF) is typically defined as a measurable quantity, being a spectral integral over a waveband. BRF is defined as

$$BRF_\lambda\left(\Omega(\theta_v,\varphi_v);\Omega'(\theta_i,\varphi_i)\right) = \frac{L_{\lambda,v_{\mathrm{target}}}\left(\Omega(\theta_v,\varphi_v);\Omega'(\theta_i,\varphi_i)\right)}{L_{\lambda,v_{\mathrm{Lambertian}}}\left(\Omega(\theta_v,\varphi_v);\Omega'(\theta_i,\varphi_i)\right)} \quad (2)$$

i.e., the radiance from a target $L_{\lambda,v_{\mathrm{target}}}(\Omega(\theta_v,\varphi_v);\Omega'(\theta_i,\varphi_i))$ divided by the radiance that would be received from a perfect Lambertian target under identical illumination conditions, $L_{\lambda,v_{\mathrm{Lambertian}}}(\Omega(\theta_v,\varphi_v);\Omega'(\theta_i,\varphi_i))$. BRF is a unitless number. Where we describe reflectivity below, we refer to BRF.

The NHS is merely a special case of a hotspot observation where both view and illumination are coincident and at nadir. Thus, to characterize the likely range of reflectivity a spaceborne lidar instrument will encounter from the terrestrial land surface, it is not sufficient to merely examine values recorded by other sensors, as these are typically not made at a hotspot configuration (never mind the NHS). There are relatively few spaceborne sensors capable of sampling the BRDF: SPOT-VGT and CHRIS-PROBA have pointing capabilities; MISR and ASTER [in the visible–near-infrared (NIR)] have multiple cameras; POLDER and POLDER-II had a large imaging array; and AVHRR, MODIS, and some geostationary instruments can use overlapping wide swaths to generate composite views from different angles over time [10].

However, even sensors that sample the BRDF relatively well still do not typically sample at the NHS. Overpass times are constrained by orbital requirements and are very unlikely to allow nadir illumination (local solar noon) except perhaps very occasionally at latitudes close to the equator. As a result, existing reflectance observations cannot be used directly to infer what a spaceborne lidar instrument would record. Therefore, without, for example, airborne observations with the same instrument characteristics (wavelengths, footprint size, etc.) as a proposed lidar, some other method is required to estimate lidar reflectivity values for a particular spaceborne lidar configuration.

Here, we propose two methods to estimate lidar reflectivity. The first method uses existing observations from POLDER and MODIS combined with angular and spectral models to interpolate these observations to the angular and spectral configurations required for a lidar instrument. The second method uses detailed 3-D models of structurally and radiometrically realistic vegetated scenes combined with Monte Carlo ray tracing (MCRT) to simulate the lidar response "directly" [11]. We then use the 3-D modeling approach to validate the first method by generating simulated POLDER and MODIS "observations" (ignoring atmospheric contributions given that the POLDER and MODIS data are atmospherically corrected). The first method mentioned earlier is then applied to these "observations," and the resulting predicted reflectivity compared with the known lidar reflectivity (from the second method). This allows the accuracy and uncertainty of the first method to be quantified. We also show how the 3-D modeling can be used to explore the impact of potential lidar observation configurations on the lidar parameter retrieval.

II. Methods

Two independent methods are presented to predict spaceborne lidar reflectivity. Unless specified otherwise, we assume a spaceborne lidar with a 100 m at full-width half-maximum (FWHM) footprint with a Gaussian point spread function (PSF). The viewing angle is specified to be 2° off-nadir rather than precisely in the NHS in order to prevent specular effects over water saturating the instrument. We assume the lidar "off" and "on" (within a CO_2 absorption feature) pulse bands to be at 1570 and 2050 nm, respectively (with a nominal bandwidth of 1 nm). For a spaceborne DIAL, these wavebands will, in practice, be determined by atmospheric absorption features—these two bands have been proposed as suitable for an instrument designed for measuring CO_2 [2].

A. Method 1: Lidar Reflectivity via POLDER and MODIS Data

Multiangular observations from the POLDER BRF database are used to provide angular sampling of the BRF [12]. We then use an angular (BRDF) model to extrapolate these observations (in the angular sense) to estimate what POLDER would observe were it able to view in the NHS. POLDER BRF observations, however, are limited to the visible and NIR wavebands, with a longest wavelength at 865 nm. In order to estimate reflectivity at the longer wavelengths required for a spaceborne lidar, we use MODIS reflectance samples made at (or close to) nadir view but off-nadir sun angles (frequently occurring) to extend the POLDER-estimated NHS reflectance values to the MODIS bands closest to the desired lidar bands (1640 and 2130 nm). Finally, we use a regression model derived from hyperspectral observations to predict the values of lidar reflectivity at 1570 and 2050 nm from reflectivity estimated at the MODIS bands.

POLDER BRF observations were collated for six cover types chosen from the GLC2000 Land Cover product to span a wide range of surface brightness variation [13]. Each POLDER observation within the selected cover type was located in the contemporaneous MODIS 8-day reflectance product MOD09A1 (500-m resolution) [14]. The MODIS tile for each cover

TABLE I
GLC2000 LAND COVER CLASSES USED

GLC class	GLC Cover Type	N_{obs}	N_{obs} PP
01	Tree cover, broadleaf, evergreen	987	987
02	Tree cover, broadleaf, deciduous	2003	220
04	Tree cover, needle-leaf, evergreen	6639	4212
14	Sparse herbaceous/shrub cover	4280	3824
16	Cultivated and managed areas	1998	917
21	Snow and ice	1532	1460

TABLE II
LOCATION OF EACH SELECTED COVER TYPE
(http://modis-land.gsfc.nasa.gov/MODLAND_grid.htm)

GLC class	Latitude	Longitude	MODIS tile ID
01	-15.6944	-72.8599	h10 v10
02	56.8611	70.8922	h21 v03
04	37.8611	-114.875	h08 v05
14	68.3056	-141.461	h12 v02
16	60.9167	22.9143	h19 v02
21	42.75	-120.492	h09 v04

type with the highest number of POLDER observations was then used to select MODIS observations coincident with the POLDER observations in both space and time. A 12×12 region of 500-m MODIS pixels covering each 6.2-km POLDER pixel was used to generate coincident estimates of POLDER and MODIS BRF, with corresponding view and illumination angles. The MODIS pixel with the highest frequency of occurrence of good quality data within each POLDER pixel (as specified in the QA flags) was then used in the analysis. Table I shows the cover types used, their label within the GLC2000 product, the number of available POLDER and MODIS observations of each cover type over the time period of POLDER data (April–October 2003), i.e., $N_{\rm obs}$, and the number of observations within 10° relative azimuth of the solar principle plane, i.e., $N_{\rm obs}PP$. This is where the maximum hotspot variation occurs (although all observations are used in the analysis hereinafter). Table II shows the location (latitude and longitude) of the POLDER observations used and the ID of the corresponding MODIS MOD09A1 tile.

1) Angular Interpolation/Extrapolation: The POLDER data provide perhaps the most comprehensive sampling of surface BRF available from a spaceborne sensor, with many samples at or close to a hotspot configuration, but none at NHS. We define an "enhancement factor" (EF), which expresses the difference in reflectivity observed by POLDER $\rho_{\rm POLDER}$ if it were able to view at the NHS, compared with observing at the view and illumination configuration of MODIS over the same points on the surface. EF is defined as

$$EF = \frac{\rho\text{POLDER}(\theta_{i,v} \approx 0, \phi_{\rm relative} = 0)}{\rho\text{POLDER}(\theta_{i,v,\rm MODIS}, \phi_{\rm relative,MODIS})} \quad (3)$$

where the numerator is the POLDER-observed reflectivity, extrapolated to the NHS via BRDF modeling; the denominator is the POLDER reflectivity predicted at the MODIS observation angles; and $\phi_{\rm relative}$ is the relative azimuth angle between the view and illumination vectors. By calculating EF, we can then calculate lidar reflectivity as follows:

$$\rho_{\rm DIAL}(\theta_{i,v} \approx 0, \phi_{\rm relative} = 0) = EF\rho_{\rm DIAL}(\theta_{i,v,\lambda,\rm MODIS}, \phi_{\rm relative,MODIS}) \quad (4)$$

where $\rho_{\rm DIAL}(\theta_{i,v,\lambda,\rm MODIS}, \phi_{\rm relative,MODIS})$ is the reflectivity at the lidar wavebands, predicted from the MODIS observations (angles and wavebands) via spectral interpolation (see below).

The EF approach assumes that the difference in reflectivity observed at the NHS from a hotspot configuration elsewhere will be due purely to the change in viewing and illumination geometry. It is further assumed that within a given cover type, the change in reflectivity will largely be one of magnitude rather than a change in the BRDF angular "shape," i.e., BRDF shape within a cover type is similar but between cover types is different. This approach has been shown to be valid for a range of sensors and cover types [15]–[18], although a theoretical basis for this assumption has yet to be fully developed. Equation (4) assumes that the EF calculated from POLDER observations can be applied at the scale of MODIS observations. Bacour and Breon [18] suggest that the landscape at POLDER spatial resolutions is likely to be more thematically homogeneous than at finer spatial scales, which is one source of uncertainty in applying (4). Furthermore, (4) assumes that the NHS reflectance calculated from MODIS (with directional information from POLDER) will produce a reasonable estimate at the proposed DIAL instrument resolution, whereas Pinty *et al.* [19] note that the BRDF "shape" can depend on the scale of observations. We note that the expected range of reflectance at the DIAL resolution is likely to be larger than the lower resolution MODIS data, so estimates of DIAL reflectance from (4) are likely to be an underestimate. This is further investigated below via radiative transfer modeling and dealt with through assuming a model inadequacy term in predicting DIAL reflectivity.

To calculate the EF defined in (3), we require a model of BRF which can, given samples at a range of view and illumination angles, predict reflectivity at other arbitrary view and illumination angles (in particular, the NHS). Here, we use the semiempirical BRF model of [20], which describes the BRF of arbitrary surface as a function of the viewing and illumination geometry plus a small number of parameters describing the surface anisotropy. Although it can be phrased in a (log-transformed) linear form [21], we invert the model against POLDER and MODIS observations here using iterative numerical inversion (Powell direction set). The inversion yields estimates of the model parameters describing surface anisotropy which can then be used to model reflectivity at any viewing and illumination geometry (for a given surface), with an estimate of the uncertainty in extrapolation (increasing with angular distance of the forward-modeled predictions away from the observation geometry at which the model was inverted). The application of the angular model allows predictions of POLDER reflectivity at the NHS to be inferred from observations made away from the NHS.

POLDER observations are made at five wavelengths (443, 565, 670, 765, and 865 nm). Uncertainty values (1σ) in POLDER observations at each waveband are assumed to be 0.006, 0.008, 0.008, 0.030, and 0.030, twice the values cited in [22] for nearby MODIS wavebands. This is expected to be a conservative (high) estimate of uncertainty.

2) Spectral Interpolation: From examination of a wide range of laboratory and field-measured leaf, soil, snow, and canopy spectra, reflectivity at the lidar wavebands assumed here appears to be highly correlated to the nearby MODIS

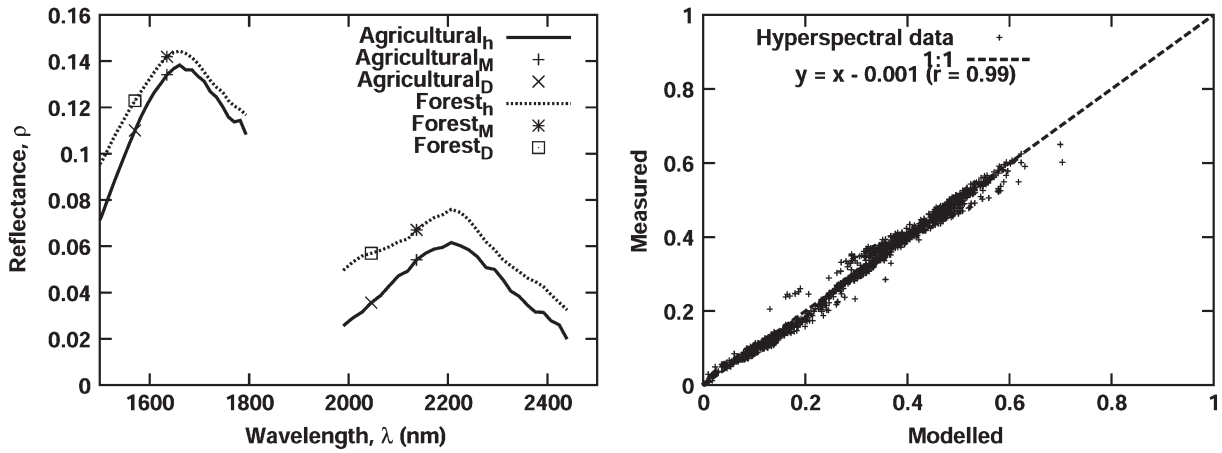

Fig. 1. (Left) Example hyperspectral data from which relationships in (5) are derived (labeled h), with location of the MODIS (M) and lidar (L) wavebands. (Right) Application of (5) to the measured hyperspectral data.

bands [23]. A multilinear regression relationship for predicting reflectivity at 1570 and 2130 nm from MODIS reflectivity at 1640 and 2130 nm was derived from these observed data

$$\begin{aligned}\rho_{\mathrm{DIAL},1570\mathrm{nm}} &= 0.727\rho_{\mathrm{MODIS},1640\mathrm{nm}} + 0.309\rho_{\mathrm{MODIS},2130\mathrm{nm}} \\ \rho_{\mathrm{DIAL},2050\mathrm{nm}} &= -0.238\rho_{\mathrm{MODIS},1640\mathrm{nm}} + 1.03\rho_{\mathrm{MODIS},2130\mathrm{nm}}.\end{aligned} \tag{5}$$

Fig. 1 shows example hyperspectral data used to derive (5) as well as the resulting regression relationships. The RMSEs of the model fit in (5) are 0.0128 (1570 nm) and 0.0274 (2050 nm), i.e., 1% and 3%, respectively. We assume the EF to be valid, irrespective of spatial resolution in the analysis, based on the averaging effects of scale on the BRDF shape (as discussed earlier).

B. Method 2: Simulating Lidar Reflectivity Using Detailed 3-D Models

Detailed 3-D canopy scenes were created, and lidar reflectivity for each scene was simulated with a 3-D MCRT model. The MCRT model used here is the *librat*[1] C library developed from the study in [24]. The model agrees very closely in tests with other numerical solutions to radiative transport in vegetation [25], [26]. Indeed, the underlying scattering model within *librat* is one of a suite of models used in a recently developed model benchmarking tool [27]. The model has also been used to reconstruct observed data [28]. Such a model requires minimal assumptions regarding the canopy structure (by comparison with simplified approaches to solving the radiative transfer equation). Although a large quantity of information is required to drive such a model (the position, orientation, and scattering properties of each branch, trunk, needle, leaf, etc., within a scene), arbitrary viewing and illumination configurations and sensor characteristics (FOV, bandpass function, PSF, etc.) can be simulated as required. In addition, environmental parameters such as the sky radiance distribution and surface topography can also be included. The scattering model assumes bi-Lambertian scattering at each interaction. This precludes the consideration of coherent backscatter as discussed earlier. However, the size of the scattering elements within each scene (leaves, branches, twigs, leaves, needles, etc.) is much larger than the wavelength, so scattering is dominated by geometric effects, and coherent scattering is expected to be small [8], [9].

Three-dimensional scenes corresponding to a subset of the cover types selected earlier, namely, broadleaf deciduous (birch), evergreen needleleaf (Sitka spruce), and agricultural (wheat), were generated. Various canopy densities were simulated, providing a range of leaf area index (LAI) values. Results from "high" and "low" LAI canopies are reported hereinafter in each instance. The 3-D birch tree canopy structure was derived from the OnyxTREE software [29], with model output modified to match observed tree height and LAI in a birch forest in Sweden [30]. By varying the number of trees in the scene, different LAI values were simulated (0.22, 0.60). Three-dimensional Sitka spruce canopy structure was derived from the PINOGRAM model [31], modified as described in [28], for various LAI values from 1.6 to 2.78. Each of the conifer scenarios contains trees of varying ages from 5 to 40 years, corresponding to tree height variation from $\sim$1.5 to $\sim$35 m, respectively. Three-dimensional wheat canopy structure was derived using the ADEL-wheat model [32]. Wheat canopies of LAI 0.31 and 3.91 were simulated.

For each canopy type, a limited number of individual "plant" objects were generated (ten trees for birch; five trees each from ten age classes for spruce; five wheat plants) and then "cloned," i.e., rotated and translated in order to populate a horizontal area. For the lidar simulations, the base-level canopy extent in each case was typically 300–500 m on a side, allowing multiple simulations of a given 100-m diameter footprint within each scene. This enabled the impact of within-cover heterogeneity on simulated lidar reflectivity to be quantified. The base-level scenes were themselves (hierarchically) cloned on a grid to provide coverage over a much larger extent (several km) to ensure that edge effects (possible escape of photons from the canopy edge) did not affect simulations of the 100-m footprints. For the POLDER and MODIS samples, scenes were extended to be $>$100 km on a side to allow simulations of off-nadir view samples, where the projected ellipsoidal FOV of POLDER can increase to around 15 km in length. Fig. 2 shows examples of each canopy.

[1]Available for download by obtaining and running on UNIX (Solaris, Linux, OS X) http://www.geog.ucl.ac.uk/~plewis/bpms/src/lib/configure.

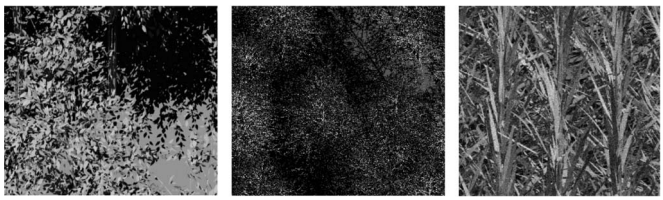

Fig. 2. (Left) Birch canopy of LAI 0.3, showing an area of $\sim 1 \times 1$ m. (Center) Sitka spruce canopy of LAI 2.2, showing an area of $\sim 10 \times 10$ m. (Right) Wheat canopy LAI 1.4, showing an area of $\sim 0.3 \times 0.3$ m.

The scattering behavior of a particular scene and configuration (view and illumination, FOV, and PSF) is calculated using reverse MCRT [9], as the number of interactions of a given "photon" (ray) from the detector, escaping the scene along a path to the illumination source, with each of the scene scattering elements. At each scattering interaction (over some finite number of scattering orders, typically 100), the incoming ray energy is attenuated by the material spectral scattering (reflectance and transmittance) properties. Scene reflectance is then calculated as the sum over all scattering orders of all possible interactions of these individual interactions. The scattering path is calculated once only for a given angular and structural configuration, and then, arbitrary spectral scattering properties can be used to calculate scene reflectance for given waveband and material spectral properties.

Here, reflectance (and transmittance in the case of leaf and needle material) properties were specified using a range of modeled and measured spectra (leaves, woody material, needles, soil, and snow) covering a range of values (and combinations). Leaf reflectance and transmittance spectra were generated using the PROSPECT leaf model of Jacquemoud *et al.* [33] for both "wet" and "dry" conditions (high, low leaf water); "wet" soil spectra were taken from the first principle component of a wide range of soil reflectance spectra [34], representing a "typical" dark wet soil and, multiplied by two, a "typical" bright wet soil; dry soil reflectance was taken from the study in [35] (although this is a particularly bright spectrum); a pure snow spectrum for snow particle radius of 100 μm was generated from the snow model of Stamnes *et al.* [36]. Fig. 3 shows the various spectra used.

The spectra in Fig. 3 were used in various combinations, referred to subsequently as follows: dry soil, dry leaf (DSDL); dry soil, wet leaf (DSWL); soil principle component, dry leaf (PSDL); soil principle component, wet leaf (PSWL); soil principle component bright, dry leaf (PSBDL); soil principle component bright, wet leaf (PSBWL); snow, dry leaf (SDL); and snow, wet leaf (SWL). Some of these are less likely to occur than others in practice, e.g., DSWL, PSBWL, and SDL. The variation of material spectra within each canopy type allowed exploration of other cover types listed in Table I, in particular snow/ice (GLC 21). The three structural types, each with two LAI cases, combined with the eight spectral combinations of leaf and soil properties, gave 48 possible structural–spectral combinations.

Lidar reflectivity (Gaussian PSF with 100-m FWHM diameter) was simulated for five instances of each scene: once at the center (0, 0) and then once at the center of each quadrant in the scene, i.e., $(x/2, y/2)$, $(x/2, -y/2)$, $(-x/2, -y/2)$, and $(-x/2, y/2)$, where $x = y =$ base level scene extent. For simulations of POLDER and MODIS configurations, solar-illuminated reflectivity was assumed with a direct illumination source of infinite extent (the Sun) assumed at infinite distance in addition to an isotropic diffuse source of infinite extent (the sky). The percentage of diffuse illumination was calculated using a sky radiance model as described in [24]. For simulations of lidar reflectivity, the illumination was considered as a Gaussian source with the same dimensions as the receiver, providing a flashlight-like illumination of the footprint.

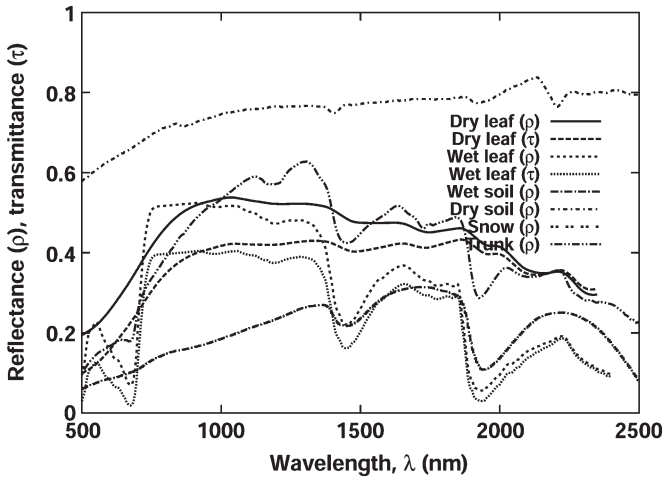

Fig. 3. Component spectra used in the 3-D MCRT simulations of lidar reflectivity and for simulating POLDER and MODIS "observations."

The relationship in (5) was used to extend spectral simulations at the POLDER and MODIS bands to lidar bands, as in method 1. Assessment of this relationship with the 3-D MCRT simulated data shows the same good agreement as for the measured spectra ($r = 0.99$ and $RMSE < 0.03$). These 3-D MCRT-simulated observations were then treated to the same analysis as described earlier in Method 1. In this case, however, the lidar reflectivity is known from the 3-D MCRT simulations, providing an independent assessment of the accuracy of Method 1.

To demonstrate the ability of the methods presented here for assessing lidar configurations, the impact of the movement of the "on" and "off" pulses on the accuracy of lidar-retrieved CO_2 concentration, i.e., X_{CO2}, was analyzed via 3-D simulations. Here, we assume an along-track ground speed of 7 km $\cdot$ s^{-1} in orbit and a delay of 250 μs between pulses. The resulting ground shift of 1.75 m was simulated for the lidar configuration and translated to $\delta X_{\mathrm{CO2}}/X_{\mathrm{CO2}}$, the fractional error in retrieved CO_2, using

$$\frac{\delta X_{\mathrm{CO_2}}}{X_{\mathrm{CO_2}}} = \frac{1}{2\tau}\frac{\delta\rho}{\rho} \tag{6}$$

where τ is the optical thickness (assumed to be 0.79 at 1570 nm and 1.3 at 2050 nm) and $\delta\rho$ is the change of reflectance ρ caused by the pulse shift (i.e., $\delta\rho = (\rho_1 - \rho_2)/\rho_1$, where $\rho_{1,2}$'s are the reflectance of the "on" and "off" pulse footprints, respectively). Instances of the pulse shift were simulated for the various 3-D canopies described earlier. Fig. 4 shows examples of the simulated DIAL footprint for the 3-D canopy scenarios.

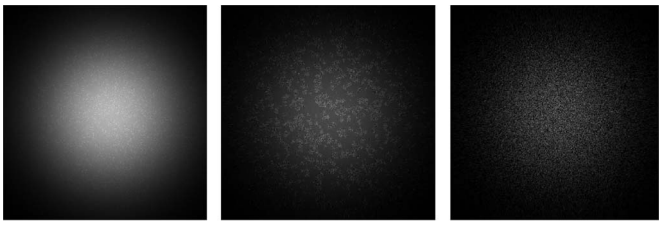

Fig. 4. MCRT simulations of lidar reflectivity of (from left to right) birch, spruce, and wheat canopies. Each scene shows the 100-m-diameter lidar-illuminated footprint. The grayscale represents a linear contrast stretch between the maximum and minimum values in each case. Spatial patterns are the 3-D canopy scenarios as viewed (and illuminated) by the lidar instrument.

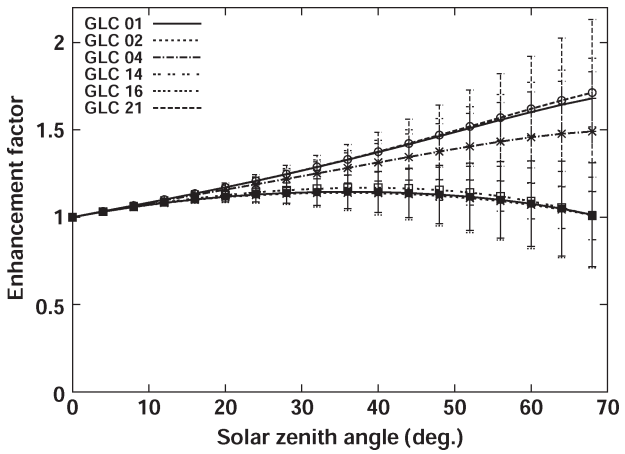

Fig. 5. Values of EF derived from POLDER observations for six cover types.

Finally, the impact of the pulse shift was assessed using five atmospherically corrected airborne HyMAP scenes over agricultural and forested areas. These are described in more detail in [28]. A 100-m FWHM diameter Gaussian PSF "footprint" was convolved with 100 randomly chosen points within each scene and then shifted by one pixel up and down, and left to right to estimate the impact of the pulse shift on reflectivity. Although these analysis data do not consider the NHS geometry, the important factor is the relative contrast between the shifted footprints rather than the absolute value in each case. In addition, the HyMAP data contain the correct lidar wavelengths, so no spectral interpolation is required.

III. Results and Discussion

Results are presented as follows: First, examples of the EF derived from fitting the BRDF model to POLDER data over all six cover types are summarized; histograms of predicted lidar reflectivity using Method 1 (POLDER and MODIS data and EF values) are shown; results from Method 2 (direct simulations of lidar reflectivity) are shown; the accuracy of Method 1 is illustrated via 3-D MCRT simulations; and finally, results for the impact of the on–off pulse shift are given.

A. Method 1: EF Values and Application to POLDER and MODIS Data

Fig. 5 shows EF values calculated from the BRDF model fitting to POLDER and MODIS data for all cover types in Table I. Error bars in Fig. 5 represent ± 1 standard deviation from EF averaged over all POLDER wavebands.

There are several points to note about the behavior of EF. First, the value of EF at nadir illumination, $\theta_i = 0^\circ$, is one by definition from (3). As θ_i increases, EF typically increases smoothly before either leveling off (GLC 04), reaching a maximum and decreasing (GLC 14, 16, 21) or continuing to rise at the same rate (GLC 01, 02). Interestingly, EF is consistent across cover types until diverging at θ_i between 20° and 30°. Spectral variation within EF is greater in the visible (not shown) with values of EF at longer wavelengths typically being higher. It is notable that although the concept of EF is meant to address the reflectivity "gain" that a spaceborne lidar would measure through viewing in the NHS, it can nevertheless fall below one, particularly for GLC 16 and 21 (cultivated and managed areas, and snow and ice, respectively). This implies that the NHS reflectivity, as predicted via the BRDF model, is actually slightly lower than that predicted at the nadir view zenith angle (but at the observed off-nadir sun angle) from the BRDF model fit. This typically occurs when the observations to which the BRDF model is fitted are made far away from nadir view or sun zenith angles, in which case the BRDF model is required to extrapolate over a large angular range (and the reflectance is generally higher anyway). The RMSE of the BRDF model fit to the POLDER observations was $1.87 \pm 0.71\%$. The fit is noticeably worse for GLC 21 (snow/ice, $2.5 \pm 0.44\%$), suggesting that the BRDF model is less appropriate for this more extreme case (where we might also expect the coherent scattering effect to become more apparent).

To quantify uncertainty in the estimates of EF, the various uncertainties in POLDER and MODIS observations and spectral interpolation were propagated through the analysis. In addition, a "model inadequacy" of 5% relative (random) error was included to represent the case that the BRDF model is just not appropriate for predicting NHS from a given set of observations. The resulting uncertainty in EF was small (always $< 5\%$ relative error) and essentially constant with solar zenith angle, showing that the 5% model inadequacy term swamped all other uncertainty.

Table III presents summary statistics of all values of EF derived from the POLDER data. EF values are typically between 1.1 and 1.33, representing the difference in lidar reflectivity due to viewing in the NHS compared with viewing away from this point, i.e., between 10% and 33% relative increase in reflectivity. There are some much higher values, but relatively few as demonstrated by the variance.

TABLE III
Summary of EF Values for Six Cover Types, Averaged Across All Bands

GLC class	Mean	1σ	10^{th} %ile	90^{th} %ile
01	1.33	.03	0.70	2.29
02	1.10	.07	0.51	1.68
04	1.29	.04	0.44	2.64
14	1.17	.03	0.12	4.82
16	1.15	.03	0.50	1.81
21	1.33	.08	0.98	3.34

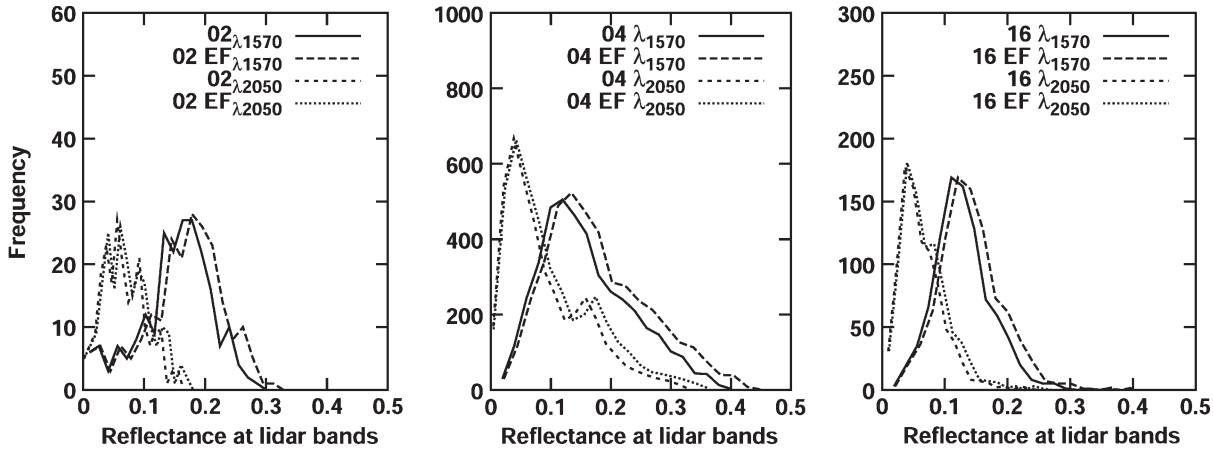

Fig. 6. Histograms of lidar reflectivity at 1570 and 2050 nm predicted from POLDER and MODIS observations for three cover types (GLC 02, 04, and 16), both before and after application of EF values.

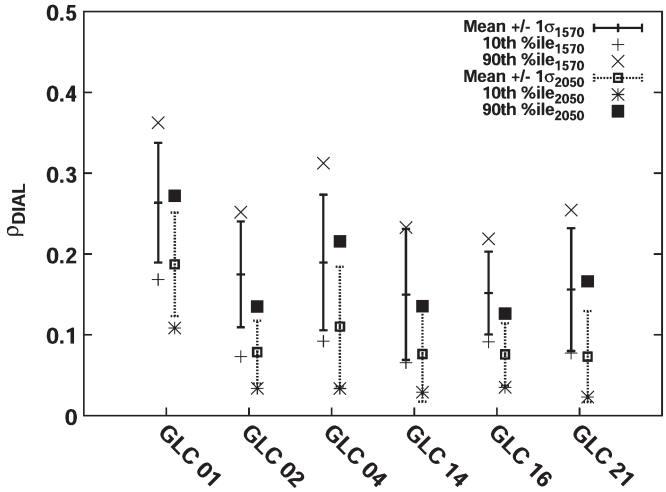

Fig. 7. Mean and standard deviation of lidar reflectivity for six cover types, with 10th and 90th percentile values. Values on the left in each case are for 1570 nm; values on the right are for 2050 nm.

The values of EF calculated for each POLDER data set were applied to the corresponding MODIS observations. Following the application of (5), histograms of the resulting DIAL reflectance were produced. Examples from cover types GLC 02, GLC 04, and GLC 16 (representing broadleaf, conifer, and agricultural) are shown in Fig. 6. Behavior of the other three cover types is similar. Unsurprisingly, given the values of EF in Table III, the histograms of the pre- and postapplications of the EF values are similar. The upper and lower values of the predicted lidar reflectivity, which determine the likely dimensions of spaceborne lidar instrument optics (lower value) and dynamic range, are summarized in Fig. 7. The 10th and 90th percentile values are shown rather than the absolute minimum and maximum values as there are a small number of extreme values (close to zero and one, respectively), but these were assumed to be outliers. In any case, it is the "typical" values which were of interest. By using these limits, the highest and lowest values of lidar-predicted reflectance from POLDER and MODIS data are 0.023 (GLC 21, 2050 nm) and 0.36 (GLC 01, 1570 nm). In practice, we can expect values measured by a lidar at the NHS to lie between these limits 80% of the time,

TABLE IV
MEAN VALUES OF LIDAR REFLECTIVITY SIMULATED VIA 3-D MCRT FOR THREE CANOPIES, AT HIGH AND LOW LAI, FOR TWO COMBINATIONS OF SCENE SPECTRA, DSDL AND SWL

	Birch			Spruce		
	LAI	DSDL	SWL	LAI	DSDL	SWL
1570nm	0.22	0.74	0.16	1.63	0.78	0.08
	0.46	0.62	0.21	2.78	0.75	0.10
2050nm	0.22	0.65	0.05	1.63	0.79	0.02
	0.46	0.48	0.06	2.78	0.73	0.03

	Wheat		
	LAI	DSDL	SWL
1570nm	0.31	0.79	0.09
	3.90	0.48	0.19
2050nm	0.31	0.79	0.03
	3.90	0.35	0.06

with the remaining 20% of the time bringing the possibility of saturation or an abnormally low signal. It should be stressed that, as mentioned earlier, the assumptions underlying the use of EF apply to spatial resolutions of > 100 m.

B. Method 2: 3-D MCRT Simulations

1) Simulations of Lidar Reflectivity: Table IV shows the results of the 3-D MCRT simulations of the birch, spruce, and wheat canopies. In each case, the spectral combination of DSDL and SWL yielded the highest and lowest reflectivity values. No values are given for σ in these cases, as the values are very low, being $\ll 1\%$ reflectivity in all cases (the majority $\sim$0.1%). This small variation is due to the relative lack of structural heterogeneity in the 3-D scenes at the resolution simulated—each scene is composed of one cover type only. Regardless of the range of variation within that cover type, it is likely to be less variable than an observed pixel of up to 6.2 km in the case of POLDER. The comparatively large range of reflectivity variation between cover types and between the DSDL and SWL cases is almost solely due to the spectral characteristics of the scene components (leaf, branch, background, etc.).

Table IV shows that the lowest value of the predicted lidar reflectivity is 0.02 (spruce, 2050 nm LAI 1.63, SWL), which is virtually identical to the values derived from the POLDER observations above. The upper values, however, of $\sim$0.79 (spruce

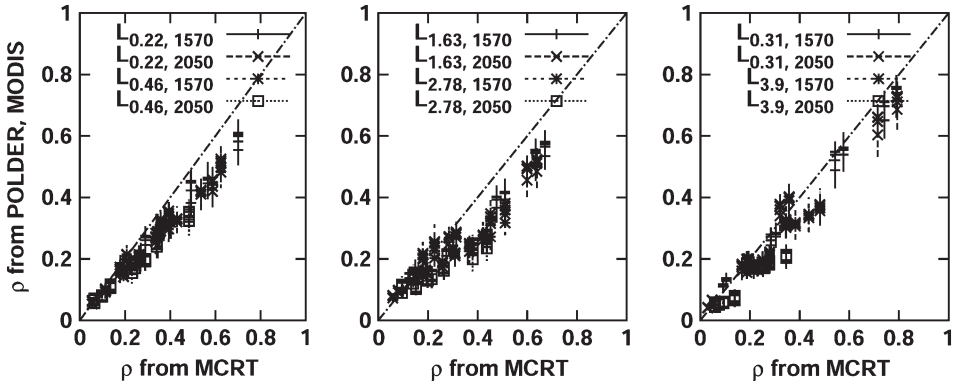

Fig. 8. Scatter of predicted lidar reflectivity values derived from Method 1 (POLDER and MODIS observations) against those derived from Method 2 (3-D MCRT-simulated POLDER and MODIS observations). (Left) Birch (LAI 0.22, 0.46). (Middle) Sitka (LAI 1.63, 2.78). (Right) Wheat (LAI 0.31, 3.9). Error bars represent $\pm 1\sigma$ over all wavebands. The multiple points at each x value are the various combinations of scene spectral components.

and wheat, 1570 and 2050 nm, low LAI, DSDL) are much higher than the POLDER-derived upper values (0.33). This is due to the dry soil spectra being particularly bright (see Fig. 3). If the PSBDL case is considered instead, the maximum reflectivity values fall to $\sim$0.5 for 1570 nm and $\sim$0.36 for 2050 nm. This suggests that the low values are likely to be well characterized (with close agreement between POLDER-predicted and 3-D MCRT-simulated values), whereas the upper values could be as high as 0.7 but will generally lie between 0.3 and 0.5.

2) Test of Method 1 via 3-D MCRT Simulations of POLDER and MODIS Observations: Fig. 8 compares lidar reflectivity predicted from Method 1 (POLDER- and MODIS-derived values of EF), with values generated from simulating POLDER and MODIS samples and then analyzing these "observations" in the same way. In this latter case, the "true" lidar reflectivity (for a given 3-D scene) is known from the simulations described earlier. Comparisons are presented for all 48 structural–spectral combinations described earlier, separated into the three structural canopy types.

The mean R^2 for the comparisons is 0.95, with a lowest value of 0.85 (Sitka, LAI 2.68, 1570 nm). The 3-D MCRT-simulated values are generally slightly lower than the values generated from the POLDER and MODIS "observations." This indicates that the two methods agree well, i.e., the methods are consistent, but the POLDER- and MODIS-derived values are a slight underestimate. The agreement is encouraging in that it suggests that the method of estimating lidar reflectivity from existing data is acceptable (for spatial resolutions of 100 m or more). The fact that the POLDER- and MODIS-derived values are consistently slightly lower than the true values and the fact that 5% BRF model "inadequacy" dominates errors in this method (see above) suggest that the addition of random error is not appropriate, as the offset is consistent, i.e., there is a slight bias ($< 10\%$). This indicates a possible bias in the BRF-model predictions of NHS reflectivity, possibly due to the model being required to extrapolate quite large angular distances away from where observations were made.

3) Simulating the Impact of Lidar On–Off Pulse Delay: The changes of $\delta\rho$ resulting from the footprint shift of 1.75 m between the 3-D MCRT-simulated on–off pulses were used with (6) to estimate the impact on $\delta X_{\mathrm{CO2}}/X_{\mathrm{CO2}}$, the accuracy of retrieved CO_2 concentration. $\delta X_{\mathrm{CO2}}/X_{\mathrm{CO2}}$ was between $1.6 \pm 1.8 \times 10^{-4}$ and $15.8 \pm 7.4 \times 10^{-4}$ (1570 nm), and $1.5 \pm 2.1 \times 10^{-4}$ and $8.8 \pm 6.1 \times 10^{-4}$ (2050 nm). This error $\varepsilon(\delta X_{\mathrm{CO2}}/X_{\mathrm{CO2}})$ is shown in Fig. 9. The range of values of ε implies that, for this particular lidar configuration, the on–off pulse delay could have an impact on retrieval accuracy of X_{CO2} of up to 0.007, i.e., 0.07%. This is likely to be much lower than the required accuracy of a lidar of this sort, which might typically be 0.5%–1% [3]. Footprints of arbitrary size can be simulated easily to examine the impact on ε for example. Smaller footprints will tend to exacerbate ε as the fractional size of the footprint shift in relation to the footprint size itself will be larger.

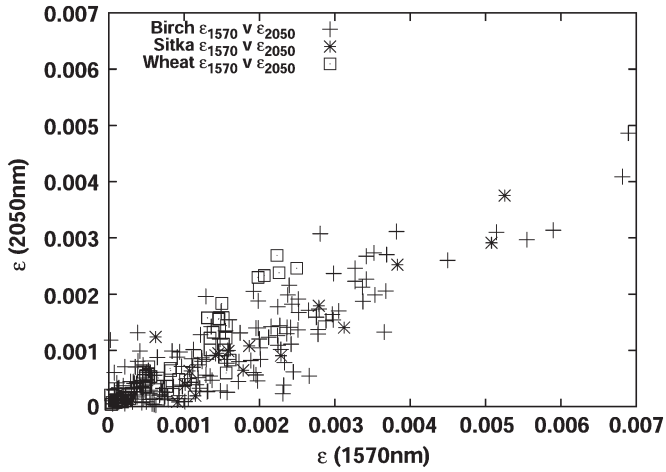

Fig. 9. Impact of on–off pulse shift on $\varepsilon(\delta X_{\mathrm{CO2}}/X_{\mathrm{CO2}})$ the error in X_{CO2}, the lidar-retrieved CO_2 concentration. The error is shown as the scatter between the values for the 1570- and 2050-nm bands because in a practical retrieval, reflectivity of the on pulse is compared with that of the off pulse, i.e., ε is a function of reflectivity in both bands. As a result, it makes sense to view ε in terms of the error in both bands simultaneously.

Results from the empirical analysis of HyMAP image data indicate that the on–off pulse shift results in values of $\delta X_{\mathrm{CO2}}/X_{\mathrm{CO2}}$ between 13 ± 16^{-4} and 51 ± 114^{-4} (1570 nm), and 16 ± 20^{-4} and 40 ± 74^{-4} (2050 nm) (between 0.01% and 0.4% X_{CO2}). This is broadly consistent with the 3-D simulations, although somewhat higher. This is partly due to the larger horizontal shift in the HyMAP data (4-m pixel size is the minimum shift) than that specified for the lidar (1.75 m). This

allows larger possible fractional changes in reflectance between the on and off pulses. In addition, the HyMAP scenes are more spatially heterogeneous than the 3-D RT simulations, as they contain a mix of cover types. This example illustrates how the 3-D MCRT simulation tools can be used to explore the impact of instrument configuration on performance.

IV. Conclusion

We have demonstrated two independent methods for estimating spaceborne lidar reflectivity and shown that the two methods agree well. We are able to characterize lidar reflectivity for a range of cover types based on existing observations. Perhaps, more importantly, we have shown that it is possible to use realistic highly detailed 3-D canopy models to simulate instrument response for a range of instrument configurations. This not only enables the validation of the method based on existing observations but also demonstrates the utility of such a method for more general exploration of instrument configurations for lidar sensing of the terrestrial surface. Although we have explored a particular set of instrument characteristics here, both methods we have presented are suitable for more general exploration of instrument characteristics. We have shown, for example, that the 3-D model simulations can be used for estimating the impact of lidar pulse configuration. Future scoping studies of instrument performance can use such methods to make informed decisions regarding the impact of footprint size, vertical pulse resolution, and choice of wavelength on retrieved surface and atmospheric properties.

References

[1] E. V. Browell, S. Ismail, and W. B. Grant, "Differential absorption lidar (DIAL) measurements from air and space," *Appl. Phys. B, Photophys. Laser Chem.*, vol. 67, no. 4, pp. 399–410, Oct. 1998.

[2] [Online]. Available: http://www.esa.int/esaLP/ESADQ0UHN6D_LPfuturemis_0.html

[3] T. Nishizawa, N. Sugimoto, I. Matsui, A. Shimizu, B. Tatarov, and H. Okamoto, "Algorithm to retrieve aerosol optical properties from high-spectral-resolution lidar and polarization mie-scattering lidar measurements," *IEEE Trans. Geosci. Remote Sens.*, vol. 46, no. 12, pp. 4094–4103, Dec. 2008.

[4] B. Koetz, F. Morsdorf, G. Sun, K. J. Ranson, K. Itten, and B. Allgower, "Inversion of a lidar waveform model for forest biophysical parameter estimation," *IEEE Trans. Geosci. Remote Sens.*, vol. 3, no. 1, pp. 49–53, Jan. 2006.

[5] D. Crisp, R. M. Atlas, F.-M. Breon, L. R. Brown, J. P. Burrows, P. Ciais, B. J. Connor, S. C. Doney, I. Y. Fung, D. J. Jacob, C. E. Miller, D. O'Brien, S. Pawson, J. T. Randerson, P. Rayner, R. J. Salawitch, S. P. Sander, B. Sen, G. L. Stephens, P. P. Tans, G. C. Toon, P. O. Wennberg, S. C. Wofsy, Y. L. Yung, Z. Kuang, B. Chudasama, G. Sprague, B. Weiss, R. Pollock, D. Kenyon, and S. Schroll, "The orbiting carbon observatory (OCO) mission," *Adv. Space Res.*, vol. 34, no. 4, pp. 700–709, 2004.

[6] W. Wanner, A. Strahler, B. Hu, P. Lewis, J.-P. Muller, X. Li, C. Schaaf, and M. Barnsley, "Global retrieval of bidirectional reflectance and albedo over land from EOS MODIS and MISR data: Theory and algorithms," *J. Geophys. Res.*, vol. 102, no. D14, pp. 17 143–17 162, 1997.

[7] B. Hapke, "Bidirectional reflectance spectroscopy: 4. The extinction coefficient and the opposition effect," *Icarus*, vol. 67, no. 2, pp. 264–280, Aug. 1986.

[8] B. Hapke, *Topics in Remote Sensing 3: Theory of Reflectance and Emittance Spectroscopy*. Cambridge, U.K.: Cambridge Univ. Press, ch. 8, pp. 228–235.

[9] P. Bruscaglioni, C. Flesia, A. Ismaelli, and P. Sansoni, "Multiple scattering and lidar returns," *Pure Appl. Opt.*, vol. 7, no. 6, pp. 1273–1287, Nov. 1998.

[10] S. Liang, A. H. Strahler, M. J. Barnsley, C. C. Borel, S. A. W. Gerstl, D. J. Diner, A. J. Prata, and C. L. Walthall, "Multiangle remote sensing: Past, present and future," *Remote Sens. Rev.*, vol. 18, no. 2–4, pp. 83–103, 2000.

[11] M. I. Disney, P. Lewis, and P. R. J. North, "Monte Carlo methods in optical canopy reflectance modelling," *Remote Sens. Rev.*, vol. 18, pp. 163–196, 2000.

[12] R. Lacaze, *POLDER-2 Land Surface Level-3 Products, User Manual, Algorithm Description and Product Validation*, 2005, Medias-France. Issue 1, Revision 4. [Online]. Available: http://postel.mediasfrance.org/Download/

[13] *Global Land Cover 2000 Database*, 2003, Eur. Commission, Joint Res. Centre, Ispra, Italy. [Online]. Available: http://www-gem.jrc.it/glc2000

[14] [Online]. Available: http://lpdaac.usgs.gov/modis/mod09a1v5.asp

[15] N. Strugnell and W. Lucht, "An algorithm to infer continental-scale Albedo from AVHRR data, land cover class, and field observations of typical BRDFs," *J. Clim.*, vol. 14, no. 7, pp. 1360–1376, Apr. 2001.

[16] N. Strugnell, W. Lucht, and C. Schaaf, "A global albedo data set derived from AVHRR data for use in climate simulations," *Geophys. Res. Lett.*, vol. 28, no. 1, pp. 191–194, Jan. 2001.

[17] D. P. Roy, J. Ju, P. Lewis, M. J. Choate, C. Schaaf, and F. Gao, "Multi-temporal MODIS–Landsat data fusion for relative radiometric normalization, gap filling, and prediction of Landsat data," *Remote Sens. Environ.*, vol. 112, no. 6, pp. 3112–3130, Jun. 2008.

[18] C. Bacour and F.-M. Breon, "Variability of biome reflectance directional signatures as seen by POLDER," *Remote Sens. Environ.*, vol. 98, no. 1, pp. 80–95, Sep. 2005.

[19] B. Pinty, J.-L. Widlowski, N. Gobron, M. M. Verstraete, and D. J. Diner, "Uniqueness of multiangular measurements—Part I: An indicator of subpixel surface heterogeneity from MISR," *IEEE Trans. Geosci. Remote Sens.*, vol. 40, no. 7, pp. 1560–1573, Jul. 2002.

[20] H. Rahman, B. Pinty, and M. M. Verstraete, "Coupled surface-atmosphere reflectance (CSAR) model. II: Semiempirical surface model usable with NOAA Advanced Very High Resolution Radiometer Data," *J. Geophys. Res.*, vol. 98, no. D11, pp. 20 791–20 801, 1993.

[21] O. Engelsen, B. Pinty, M. M. Verstraete, and J. V. Martonchik, "Parametric bidirectional reflectance factor models: Evaluation, improvements and applications," EC Joint Res. Centre, Brussels, Belgium, Tech. Rep. EUR 16426 EN, 1996.

[22] D. Roy, Y. Jin, P. Lewis, and C. Justice, "Prototyping a global algorithm for systematic fire-affected area mapping using MODIS time series data," *Remote Sens. Environ.*, vol. 97, no. 2, pp. 137–162, Jul. 2005.

[23] B. Hosgood, S. Jacquemoud, G. Andreoli, J. Verdebout, and G. Pedrini, "Leaf optical properties experiment 93 (LOPEX93)," Eur. Commission, Joint Res. Centre Inst. Remote Sens. Appl., Ispra, Italy, EUR-16095-EN, 1995.

[24] P. Lewis, "The botanical plant modelling system," *Agronomie—Agric. Environ.*, vol. 19, no. 3/4, pp. 185–210, 1999.

[25] B. Pinty, J.-L. Widlowski, M. Taberner, N. Gobron, M. M. Verstraete, M. I. Disney, F. Gascon, J.-P. Gastellu, L. Jiang, A. Kuusk, P. Lewis, X. Li, W. Ni-Meister, T. Nilson, P. R. J. North, W. Qin, L. Su, S. Tang, R. Thompson, W. Verhoef, H. Wang, J. Wang, G. Yan, and H. Zang, "Radiation transfer model intercomparison (RAMI) exercise: Results from the second phase," *J. Geophys. Res.*, vol. 109, no. D6, p. D06 210, Mar. 2004. DOI: 10.1029/2003JD004252.

[26] J.-L. Widlowski, M. Taberner, B. Pinty, V. Bruniquel-Pinel, M. Disney, R. Fernandes, J.-P. Gastellu-Etchegorry, N. Gobron, A. Kuusk, T. Lavergne, S. Leblanc, P. E. Lewis, E. Martin, M. Mottus, P. R. J. North, W. Qin, M. Robustelli, N. Rochdi, R. Ruiloba, C. Soler, R. Thompson, W. Verhoef, M. M. Verstraete, and D. Xie, "The third radiation transfer model intercomparison (RAMI) exercise: Documenting progress in canopy reflectance models," *J. Geophys. Res.*, vol. 112, no. D9, p. D09 111, May 2007. DOI: 10.1029/2006JD007821.

[27] J.-L. Widlowski, M. Robustelli, M. Disney, J.-P. Gastellu-Etchegorry, T. Lavergne, P. Lewis, P. R. J. North, B. Pinty, R. Thompson, and M. M. Verstraete, "The RAMI on-line model checker (ROMC): A web-based benchmarking facility for canopy reflectance models," *Remote Sens. Environ.*, vol. 112, no. 3, pp. 1144–1150, Mar. 2008.

[28] M. Disney, P. Lewis, and P. Saich, "3D modelling of forest canopy structure for remote sensing simulations in the optical and microwave domains," *Remote Sens. Environ.*, vol. 100, no. 1, pp. 114–132, Jan. 2006.

[29] Cambridge, MA: Onyx Comput. Inc., [Online]. Available: http://www.onyxtree.com

[30] [Online]. Available: http://www.abacus-ipy.org/fieldsites/abisko.html

[31] R. P. Leersnijder, "PINOGRAM: A pine growth area model," Ph.D. dissertation, Wageningen Agric. Univ., Wageningen, The Netherlands, 1992. WAU dissertation 1499.
[32] C. Fournier, B. Andrieu, S. Ljutovac, and S. Saint-Jean, "ADEL-Wheat: A 3D architectural model of wheat development," in *Int. Symp. Plant Growth Model., Simul., Vis. Appl.*, B.-G. Hu and M. Jaeger, Eds., 2003, pp. 54–63.
[33] S. Jacquemoud, S. L. Ustin, J. Verdebout, G. Schmuck, G. Andreoli, and B. Hosgood, "Estimating leaf biochemistry using the PROSPECT leaf optical properties model," *Remote Sens. Environ.*, vol. 56, no. 3, pp. 194–202, Jun. 1996.
[34] J. C. Price, "On the information content of soil reflectance spectra," *Remote Sens. Environ.*, vol. 33, no. 2, pp. 113–121, Aug. 1990.
[35] I. Bogrekci and W. S. Lee, "The effects of soil moisture content on reflectance spectra of soils using UV-VIS-NIR spectroscopy," in *Proc. 7th Int. Conf. Precision Agric.*, 2004. CD-ROM. [Online]. Available: http://www.agen.ufl.edu/~wlee/Publications/2004-PAConference-63-Bogrekci-Lee.pdf
[36] K. Stamnes, S.-C. Tsay, W. Wiscombe, and K. Jayaweera, "Numerically stable algorithm for discrete-ordinate-method radiative transfer in multiple scattering and emitting layered media," *Appl. Opt.*, vol. 27, no. 12, pp. 2502–2509, 1988.

Mathias I. Disney received the B.Sc. degree in physics from the University of Bristol, Bristol, U.K., in 1992 and the M.Sc. and Ph.D. degrees in remote sensing from the University of London, London, U.K., in 1995 and 2000, respectively.

Since 2003, he has been a Lecturer in remote sensing with the Department of Geography, University College London, London, and is part of the Natural Environment Research Council's National Centre for Earth Observation.

Philip E. Lewis received the B.Eng. degree in avionics and the M.Sc. and Ph.D. degrees in remote sensing from the University of London, London, U.K., in 1987, 1988, and 1996, respectively.

He is currently a Professor with the Department of Geography, University College London, London, and a Member of the Natural Environment Research Council's National Centre for Earth Observation.

Marc Bouvet received the M.Sc. degree in remote sensing science and techniques from the University Paul Sabatier, Toulouse, France, and the Ecole Nationale Supérieure de l'Aéronautique et de l'Espace, Toulouse.

Since 2000, he has been with the Wave Interaction and Propagation Section, European Space Agency, European Space Research and Technology Centre, Noordwijk, The Netherlands.

Ana Prieto-Blanco received the degree in computer science from the University of Valladolid, Valladolid, Spain, in 1999, the B.Sc. degree (Hons.) in environmental sciences from the University of Wolverhampton, Wolverhampton, U.K., in 2004, and the Ph.D. degree in Earth observation from the University of Wales, Swansea, U.K., in 2007.

Since 2006, she has been with the Department of Geography, University College London, London, U.K., working on the ABACUS-IPY Project (Arctic Biosphere Atmosphere Coupling Across Multiple Scales).

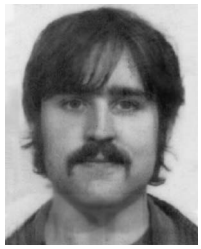

Steven Hancock received the M.Sci. degree in physics from the University of Durham, Durham, U.K., in 2005. He is currently working toward the Ph.D. degree in remote sensing in the Department of Civil, Environmental and Geomatic Engineering, the Department of Geography, and the Department of Space and Climate Physics, University College London, London, U.K., investigating the measurement of forests with waveform lidar through Monte Carlo ray tracing.